

Distributed Quantum Computing across an Optical Network Link

D. Main,* P. Drmota, D. P. Nadlinger, E. M. Ainley, A. Agrawal,
B. C. Nichol, R. Srinivas, G. Araneda, and D. M. Lucas
*Department of Physics, University of Oxford, Clarendon Laboratory,
Parks Road, Oxford OX1 3PU, United Kingdom*

Distributed quantum computing (DQC) combines the computing power of multiple networked quantum processing modules, enabling the execution of large quantum circuits without compromising on performance and connectivity^{1,2}. Photonic networks are well-suited as a versatile and reconfigurable interconnect layer for DQC; remote entanglement shared between matter qubits across the network enables all-to-all logical connectivity via quantum gate teleportation (QGT)^{3,4}. For a scalable DQC architecture, the QGT implementation must be deterministic and repeatable; until now, there has been no demonstration satisfying these requirements. We experimentally demonstrate the distribution of quantum computations between two photonically interconnected trapped-ion modules. The modules are separated by ~ 2 m, and each contains dedicated network and circuit qubits. By using heralded remote entanglement between the network qubits, we deterministically teleport a controlled-Z gate between two circuit qubits in separate modules, achieving 86 % fidelity. We then execute Grover’s search algorithm⁵ – the first implementation of a distributed quantum algorithm comprising multiple non-local two-qubit gates – and measure a 71 % success rate. Furthermore, we implement distributed iSWAP and SWAP circuits, compiled with 2 and 3 instances of QGT, respectively, demonstrating the ability to distribute arbitrary two-qubit operations⁶. As photons can be interfaced with a variety of systems, this technique has applications extending beyond trapped-ion quantum computers, providing a viable pathway towards large-scale quantum computing for a range of physical platforms.

INTRODUCTION

The potential of quantum computing to revolutionise various fields ranging from cryptography to drug discovery is widely recognised^{7,8}. However, regardless of the physical platform used to realise the quantum computer, scaling up the number of qubits while maintaining precise control and inter-connectivity is a major technical challenge^{9–11}. The distributed quantum computing (DQC) architecture, depicted in Fig. 1, addresses this challenge by enabling large quantum computations to be executed by a network of quantum processing modules^{1,2}. The modules each host a relatively small number of qubits and are interconnected via both classical and quantum information channels. By preserving the reduced complexity of the individual modules and transforming the scaling challenge into the task of building more modules and establishing an interface between them, the DQC architecture provides a scalable approach to fault-tolerant quantum computing^{3,4}.

The interface between modules could be realised by directly transferring quantum information between modules. However, losses in the interconnecting quantum channels would lead to the unrecoverable loss of quantum information. Quantum teleportation offers a lossless alternative interface, using only bipartite entanglement (e.g. Bell states) shared between modules, together with local operations and classical communication (LOCC) to effectively replace the direct transfer of quantum information across quantum channels^{12,13}. Quantum gate teleportation (QGT) efficiently implements non-local entangling gates between qubits in sep-

arate modules, consuming only one Bell pair and the exchange of two classical bits^{14,15}, as depicted in Fig. 1(b). Given arbitrary single- and two-qubit operations within each node, QGT completes a universal gate set for the distributed quantum computer¹³. The primary advantage of teleportation-based schemes over direct transfer is the exclusive use of the quantum channel for generating identical Bell states; channel losses can be overcome by repetition without losing quantum information, and the distance between modules can be increased by inserting quantum repeaters¹⁶. Additionally, channel noise may be suppressed using entanglement purification¹⁷. Since teleportation protocols are executed strictly after entanglement has been established, they enable continuous deterministic operation even if the entanglement is generated non-deterministically. This deterministic nature is crucial for the scalability, eliminating the need for post-selection of singular successful outcomes out of an exponentially large set of undesired outcomes.

Teleportation protocols are agnostic to the physical implementation of the quantum channels, making them a versatile tool for DQC across different platforms. In the trapped-ion quantum charge-coupled device (QCCD) architecture, qubits can be dynamically transported between modules within a single chip¹⁸ – or even across chips¹⁹ – and thus be used to mediate entangling gates between different trap zones^{20,21}. Photons, however, make natural carriers of quantum information since they can travel long distances without significant degradation of their quantum state. Photonic interconnects enable all-to-all connectivity between qubits distributed across the network whose topology can be dynamically recon-

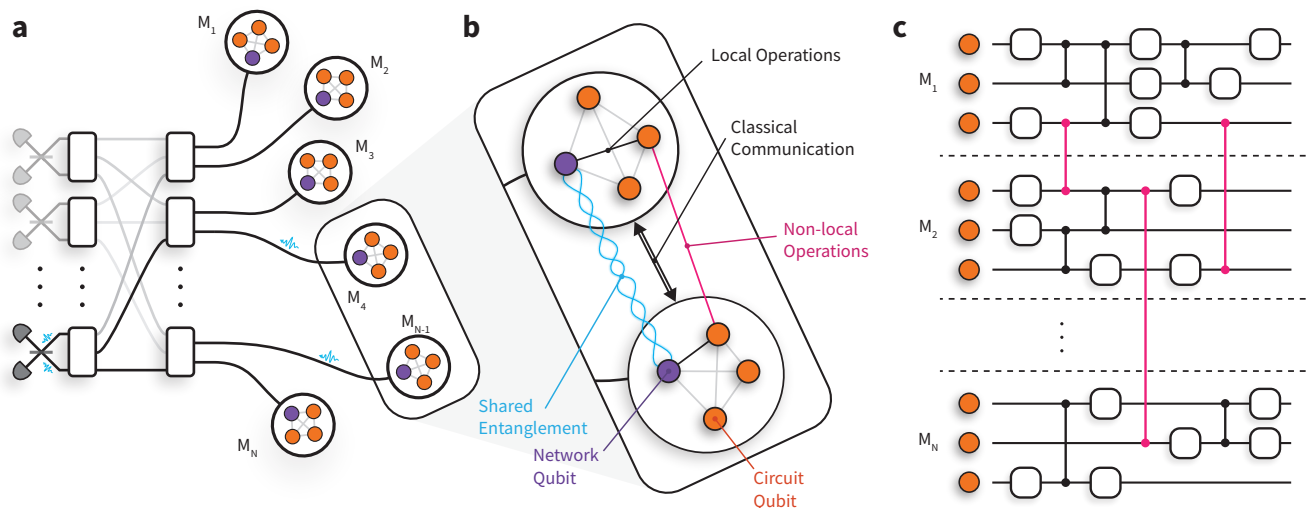


Fig. 1. Distributed quantum computing architecture. **a**, Schematic of a DQC architecture comprising photonically interconnected modules. Entanglement is heralded between network qubits via the interference of photons on beamsplitters. A photonic switchboard provides a flexible and reconfigurable network topology. **b**, The modules consist of a small number of network qubits (purple) and circuit qubits (orange), which may directly interact via local operations. Quantum gate teleportation mediates non-local gate interactions (pink) between circuit qubits in separate modules. These protocols require the resources of shared entanglement, local operations, and classical communication. **c**, A quantum circuit distributed across a network of small quantum processing modules that function together as a single, fully intra-connected quantum computer.

figured without the need to open up complex vacuum and/or cryogenic systems. Moreover, optical components are widely available and can be operated under ambient conditions. These properties make photonic interconnects particularly appealing for networking quantum computing modules, as shown in Fig. 1(a). As depicted in Fig. 1(b), we consider modules containing “network” and “circuit” qubits with full interconnectivity via local quantum operations. Remote entanglement of network qubits in separate modules is generated by the interference of photons, where reconfigurability and flexibility could be provided via a photonic switchboard. This entanglement can then be used to mediate entangling gates between the circuit qubits in different modules via QGT, enabling the network to function as a single fully connected quantum processor, as shown in Fig. 1(c). Heralded entanglement between spatially separated qubits has been achieved experimentally in a variety of platforms including diamond colour centres^{22,23}, superconducting qubits²⁴, neutral atoms^{25,26}, and trapped-ions^{27–29}.

QGT has been implemented probabilistically in purely photonic systems, requiring passive optical elements and post-selection to perform the conditional rotations that complete the gate teleportation^{30,31}. Chou *et al.*³² demonstrated deterministic teleportation of a controlled-NOT gate between two qubits encoded in the modes of two superconducting cavities on the same device, separated by ~ 2 cm, while a third cavity enabled the deterministic generation of entanglement between two trans-

mon network qubits. Recently, there have been demonstrations of QGT between superconducting qubits within a single device, demonstrating the viability of QGT to overcome nearest neighbour constraints in this architecture^{33,34}. In the trapped-ion QCCD architecture, Wan *et al.*²⁰ demonstrated QGT in which the entanglement was deterministically generated between two “network” qubits via local operations before being transported $\sim 840 \mu\text{m}$ to two separate locations within the same trap. Daiss *et al.*³⁵ demonstrated a heralded non-local entangling gate across a photonic quantum network using a photon to directly transfer quantum information between modules. However, photon loss necessarily destroys the states of the circuit qubits, rendering this scheme non-deterministic. Until now, there has been (i) no demonstration of deterministic QGT across a quantum network, and (ii) no demonstration of distributed circuits comprising multiple non-local entangling gates. In photonic platforms, this has been prevented by the inability to store the photons between interactions^{30,31}, while in the QCCD demonstration, this was limited by the decoherence of the circuit qubits during the generation of entanglement²⁰.

In this work, we present the first demonstration of DQC across a network of two trapped-ion modules, each containing a network qubit and a circuit qubit, and separated by a macroscopic distance (~ 2 m). We mediate deterministic two-qubit controlled-Z (CZ) interactions between the circuit qubits via QGT, utilizing entanglement

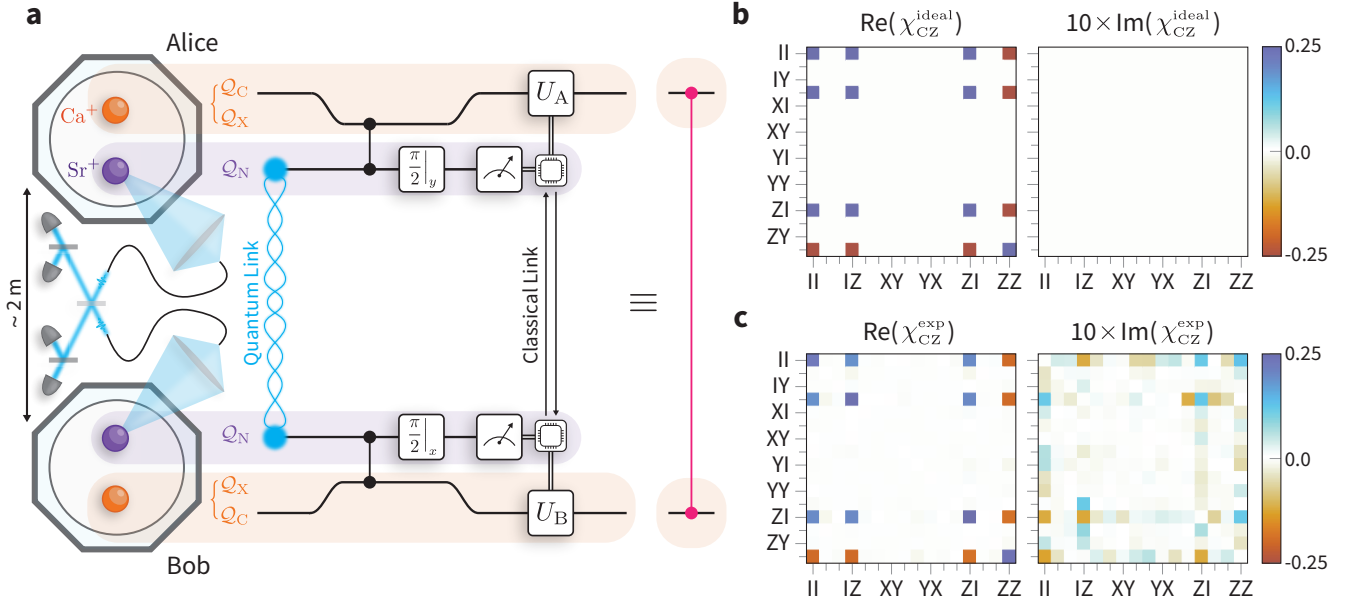


Fig. 2. Teleportation of a controlled-Z (CZ) gate between two trapped-ion modules. **a**, The two modules, Alice and Bob, each hold a $^{88}\text{Sr}^+$ ion (purple) and a $^{43}\text{Ca}^+$ ion (orange). Sr^+ provides a network qubit, Q_N , while Ca^+ provides both a long-lived circuit qubit, Q_C , and an auxiliary qubit, Q_X . Prior to the protocol, the circuit qubits are in some arbitrary state. The protocol begins by generating entanglement between the network qubits via a photonic link. Upon heralding entanglement, each module applies a local CZ gate between the network and circuit qubits, using the auxiliary qubit temporarily to mediate the gate mechanism. The outcomes of mid-circuit parity measurements of the network qubits are exchanged in real-time via a classical (TTL) link connecting the control systems of the two modules. This information is used to condition local feed-forward operations, U_A and U_B , on the circuit qubits – completing the teleportation of the CZ gate. **b**, Process matrix for an ideal CZ gate. **c**, Measured process matrix, reconstructed via quantum process tomography, yielding an average gate fidelity of 86.1(9)%, compared to an ideal CZ gate.

previously established across the network between the two network qubits. Leveraging the robust storage of quantum information in the circuit qubits while generating subsequent rounds of entanglement between network qubits³⁶, we execute distributed quantum circuits comprising multiple non-local two-qubit gates. We demonstrate the distributed iSWAP and SWAP gates, which consist of 2 and 3 instances of QGT, respectively. The actions of all teleported gates are characterized using quantum process tomography (QPT). Finally, we implement Grover’s algorithm on our distributed quantum computer.

TELEPORTATION OF A CONTROLLED-Z GATE

Our apparatus, depicted in Fig. 2(a), consists of two trapped-ion modules, Alice and Bob, each co-trapping one $^{88}\text{Sr}^+$ ion and one $^{43}\text{Ca}^+$ ion (Methods). The Ca^+ ion provides a magnetic field-insensitive “circuit” qubit, $Q_C := \{|0_C\rangle \equiv |F=4, m_F=0\rangle, |1_C\rangle \equiv |F=3, m_F=0\rangle\}$, in the ground hyperfine manifold which has been used to demonstrate state-of-the-art

quantum logic^{37,38}. The Sr^+ ion, on the other hand, provides an efficient interface to the optical quantum network²⁸. We define the network qubit in Sr^+ by $Q_N = \{|0_N\rangle \equiv |S_{1/2}, m_J = -\frac{1}{2}\rangle, |1_N\rangle \equiv |D_{5/2}, m_J = -\frac{3}{2}\rangle\}$. To implement local entangling operations between these two species, we employ the light shift gate mechanism³⁹ between Q_N and an auxiliary qubit in the ground hyperfine manifold of Ca^+ , $Q_X := \{|0_X\rangle \equiv |F=4, m_F = +4\rangle, |1_X\rangle \equiv |F=3, m_F = +3\rangle\}$, which, unlike the Q_C qubit, experiences the necessary light shifts (Methods). At the points at which we want to perform the local entangling gate, we transfer the quantum information stored in Q_C temporarily to Q_X to perform the gate operations (Methods).

The QGT protocol used here to mediate CZ gates between the circuit qubits in separate modules is depicted in Fig. 2. We allow the circuit qubits to start in an arbitrary state $|\psi_{\text{in}}^{\text{AB}}\rangle \in Q_C^{\otimes 2}$, which could be part of a larger, long-running computation. We begin the QGT protocol by generating the remotely entangled Bell state,

$$|\Psi^+\rangle = \frac{|10\rangle + |01\rangle}{\sqrt{2}} \in Q_N^{\otimes 2},$$

between the network qubits²⁸, with a fidelity of 97.15(9) % (Methods). This is done via a try-until-success process, where a herald indicates a success. The circuit qubits provide a robust quantum memory³⁶, enabling storage of the encoded quantum information until the remote entanglement is successfully heralded. At this stage, we map the state stored in the circuit qubits (\mathcal{Q}_C) to the auxiliary qubits (\mathcal{Q}_X) in preparation for the local entangling operations (Methods). In each module, we perform local CZ gates between the network and auxiliary qubits (Methods), before transferring the auxiliary qubit back to the circuit qubit. We then perform mid-circuit measurements of the network qubits in the X and Y bases in Alice and Bob, respectively. The modules exchange the measurement outcomes in real-time – using a classical (TTL) link between their control systems – and perform single-qubit feed-forward operations conditioned on the exchanged bits to complete the gate teleportation protocol (Methods). This implements the non-local gate $|\psi_{\text{in}}^{\text{AB}}\rangle \rightarrow U_{\text{CZ}}^{\text{AB}} |\psi_{\text{in}}^{\text{AB}}\rangle$.

We characterise the QGT protocol using QPT to reconstruct the process matrix, $\chi_{\text{CZ}}^{\text{exp}}$, providing a complete description of the action of the teleported CZ gate on the two circuit qubits. Compared to the ideal CZ process, shown in Fig. 2(b), the reconstructed process matrix for the teleported gate, shown in Fig. 2(c), has an average gate fidelity of 86.1(9) %. The QGT protocol is completely self-contained – the input states of the circuit qubits are set prior to the execution of the non-local gate – and output states are available for further computation. With single-qubit rotations of the circuit qubits, this teleported CZ gate is a key element of a gate set for DQC, enabling the modules to act as a single, fully-connected universal quantum processor.

DISTRIBUTED QUANTUM COMPUTING

In general, any arbitrary two-qubit unitary operation can be decomposed into at most three CZ gates⁶. We demonstrate our ability to perform sequential rounds of QGT by executing the CZ decompositions of the iSWAP and SWAP gates, shown in Figs. 3(a)(i) and 3(b)(i), comprising two and three instances of QGT, respectively. As with the teleported CZ, we characterise these circuits via QPT, see Figs. 3(a)(ii) and 3(b)(ii). From the reconstructed process matrices, we measure average gate fidelities of 70(2) % and 64(2) % for the iSWAP and SWAP gates, respectively. By constructing circuits with multiple instances of QGT – enabled by our ability to perform QGT deterministically and on-demand – we demonstrate the ability to perform universal DQC.

Finally, we implement Grover’s algorithm⁵ on our distributed quantum processor. This algorithm considers searching through a set of unsorted items, $x \in L$, to find a particular item, $a \in L$. The search problem is repre-

sented by the function

$$f_a(x) = \begin{cases} 1 & \text{if } x = a, \\ 0 & \text{otherwise.} \end{cases}$$

In the two-qubit case, there are four items to search through. Classically, the item a could be identified with, on average, two queries of the function $f_a(x)$. Using the quantum circuit shown in Fig. 3(c)(i), the same task can be accomplished with only one query. After preparing a superposition of all possible inputs with parallel Hadamard gates, an instance of QGT implements the *oracle*, which performs the mapping $U_a : |x\rangle \rightarrow (-1)^{f_a(x)} |x\rangle$, marking the state $|a\rangle$. A second instance of QGT implements the Grover *diffusion* circuit, which decodes the quantum information provided by the oracle into an observable. In the two-qubit case considered here, the application of the Grover diffusion circuit should leave the register in the state $|a\rangle$, which is the solution to the function f_a , and thus a measurement of the register yields the solution to the search problem with unit probability. In the case of N items, to approach unit probability of obtaining the solution, one would require $\sim \mathcal{O}(\sqrt{N})$ iterations of the oracle-diffusion circuit, compared with $\sim \mathcal{O}(N/2)$ for a classical search.

The results of Grover’s algorithm – executed on our distributed quantum processor – are shown in Fig. 3(c)(ii). For the marked states $a \in \{00, 01, 10, 11\}$, we obtain the correct result with an average success rate of 71(1) %. To our knowledge, this represents the first deterministic execution of any algorithm on a distributed quantum computer.

DISCUSSION

The performance of our distributed quantum circuits is consistent with the errors from the teleported CZ gates. We summarise the leading error sources affecting our teleported CZ gate in Table I. The measured fidelity of our gate is slightly lower than that predicted by the error budget, which we attribute to drifts in the calibration of various components over the duration of the data acquisition. The majority of identified error sources occur during local operations in each module. It is worth noting that our local errors do not represent the state-of-the-art of trapped-ion processors; however, local operations exceeding the fidelity threshold for fault-tolerant quantum computing have been demonstrated in this platform^{38–42}. Relevant to our implementation, Hughes *et al.*³⁹ demonstrated mixed-species two-qubit gates between $^{88}\text{Sr}^+$ and $^{43}\text{Ca}^+$ ions with a gate error of 0.2(1) %. We therefore conclude that the technical limitations in our implementation can be overcome. The other significant source of error is the remote entanglement of the network qubits across the photonic quantum network; we observe a fidelity of the remotely entangled network qubits to the

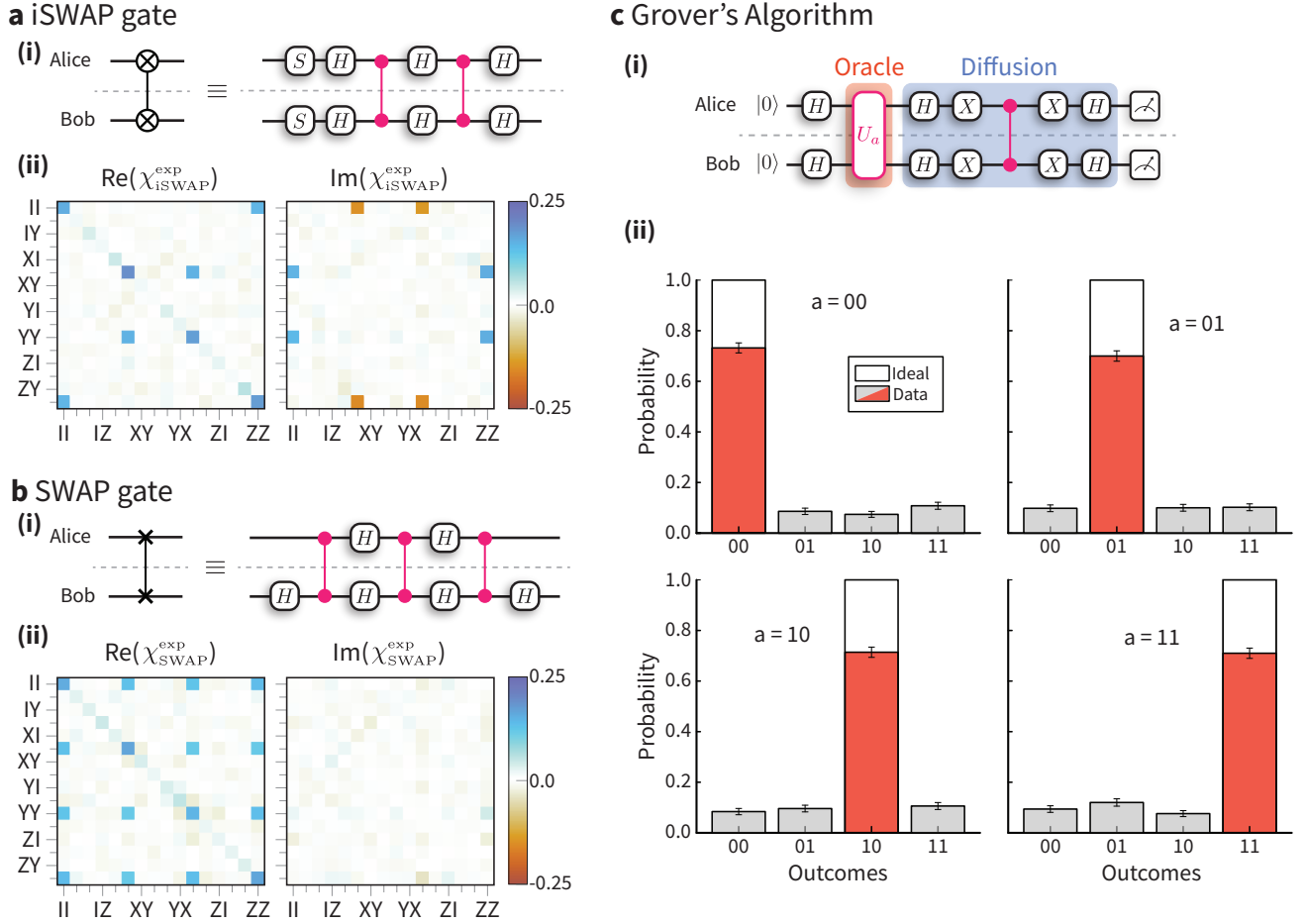


Fig. 3. Distributed quantum computing results. CZ decompositions of the distributed **a(i)** iSWAP and **b(i)** SWAP circuits, comprising two and three instances of QGT, respectively. The reconstructed process matrices for the **a(ii)** iSWAP and **b(ii)** SWAP gates indicate an average gate fidelity of 70(2) % and 64(2) %, respectively. **c**, Grover's algorithm: (i) circuit comprising two instances of QGT: the first implements the Grover oracle call which marks a particular state, a , while the second implements the diffusion circuit, (ii) measurement outcomes from 500 repetitions of Grover's algorithm per marked state; the average success probability is 71(1) %.

desired $|\Psi^+\rangle$ state of 97.15(9) %. Unlike the local operations, the performance of our remote entanglement is at the state-of-the-art. To improve this, and hence enable the teleportation of high-fidelity entangling gates between modules, entanglement purification could be used to distribute high-fidelity entangled states from a number of lower-fidelity entangled states^{17,43}.

Our implementation features a single circuit qubit in each module; however processors with larger numbers of qubits have been realised. With only 3 circuit qubits (and one network qubit) per module, the purification of arbitrary quantum channels would be possible⁴³. The capabilities of the individual modules may be extended even further by deploying the QCCD architecture. With recent demonstrations in both academic research⁴⁴ and industry²¹ highlighting the power of this approach, embedding these systems in a quantum network would com-

bine their power with the reconfigurability and flexibility of the DQC architecture. Conversely, computational bottlenecks associated with ion transport overheads observed in the QCCD architecture²¹ could be mitigated using photonic interconnects integrated into a single device⁴⁵.

While the results presented here were achieved using trapped-ion quantum processing modules, photons may be interfaced with a variety of systems. The connectivity and reconfigurability enabled by photonic networks provides a scalable approach for other quantum computing platforms such as diamond colour centres and neutral atoms. Additionally, modules of different platforms could be connected via wavelength conversion, enabling a hybrid DQC platform. Furthermore, teleportation protocols are not limited to qubits; they can be extended to higher-dimensional quantum computing paradigms,

Source	Error	
	Alice	Bob
Raw entanglement	2.85(9) %	
Mixed-species gate	2.5(2) %	2.0(2) %
\mathcal{Q}_C decoherence	1.9(4) %	1.8(5) %
$\mathcal{Q}_X \leftrightarrow \mathcal{Q}_C$ transfer	0.76(3) %	0.52(1) %
Mid-circuit measurement	0.091(3) %	0.122(2) %
\mathcal{Q}_C rotations	0.016(1) %	0.015(1) %
Predicted total error	11.9(6) %	

Table I. Error budget for CZ gate teleportation. The characterisation of each error contribution is discussed in (Methods).

such as qudits⁴⁶ and continuous-variable quantum computing (CVQC)^{47,48}, allowing these platforms to benefit from the DQC architecture. Quantum repeater technology¹⁶ would enable large physical separation between the quantum processing modules, thereby paving the way for the development of a *quantum internet*⁴⁹. The scope of these networks extends beyond quantum computing technologies; the ability to control distributed quantum systems, as enabled by this architecture, to engineer complex quantum resources has applications in multi-partite secure sharing⁵⁰, metrology⁵¹, and probing fundamental physics⁵².

METHODS

Dual-species ion-trap modules

Our apparatus comprises two trapped-ion processing modules, Alice and Bob. Each module, depicted in Ext. Fig. 1, consists of an ultra-high vacuum chamber containing a room-temperature, micro-fabricated surface Paul trap; the trap used in Alice (Bob) is a HOA2⁵³ (Phoenix⁵⁴) trap, fabricated by Sandia National Laboratories. In each module, we co-trap ⁸⁸Sr⁺ and ⁴³Ca⁺ ions. Each species of ion is addressed via a set of lasers used for cooling, state-preparation, and readout. A high-numerical aperture (0.6 NA) lens enables single-photon collection from the Sr⁺ ions. A ~ 0.5 mT magnetic field is applied parallel to the surface of the trap to provide a quantisation axis.

As outlined in the main text, the Sr⁺ ion provides an optical network qubit, \mathcal{Q}_N , which is manipulated directly using a 674 nm laser. The ground hyperfine manifold of the Ca⁺ ion provides a circuit qubit, \mathcal{Q}_C . At ~ 0.5 mT, the sensitivity of the \mathcal{Q}_C qubit transition frequency to magnetic field fluctuations is 122 kHz mT⁻¹, i.e. ~ 2 orders of magnitude lower than that of the \mathcal{Q}_N qubit – making it an excellent memory for quantum in-

formation³⁶. Additionally, we define an auxiliary qubit, \mathcal{Q}_X , in the ground hyperfine manifold of Ca⁺ for implementing local entangling operations, state preparation, and readout. The measured state-preparation and measurement (SPAM) errors for each qubit are presented in Ext. Fig. 2.

The spectral isolation between the two species allows us to address one species without causing decoherence of the quantum information encoded in the other species. We make use of this for sympathetic cooling, mid-circuit measurement, and interfacing with the quantum network during circuits.

Quantum process tomography

The action of a quantum process acting on a system of N qubits may be represented by the process matrix $\chi_{\alpha\beta}$ such that,

$$\mathcal{E}(\rho) = \sum_{\alpha,\beta=0}^{D-1} \chi_{\alpha\beta} P_{\alpha} \rho P_{\beta}^{\dagger},$$

where $P_{\alpha} \in \mathcal{P}^{\otimes N}$ are the set of single-qubit Pauli operators $\mathcal{P} = \{\mathbb{I}, \sigma_x, \sigma_y, \sigma_z\}$, and $D = \dim(\mathcal{P}^{\otimes N}) = 4^N$. QPT enables us to reconstruct the matrix $\chi_{\alpha\beta}$, thereby attaining a complete characterisation of the process.

QPT is performed by preparing the qubits in the states $\rho_i = |\psi_i\rangle\langle\psi_i|$, where $|\psi_i\rangle$ are chosen from a tomographically complete set

$$|\psi_i\rangle \in \left\{ |0\rangle, |1\rangle, \frac{|0\rangle + |1\rangle}{\sqrt{2}}, \frac{|0\rangle + i|1\rangle}{\sqrt{2}} \right\}, \quad (1)$$

performing the process, \mathcal{E} , followed by measuring the output state $\mathcal{E}[\rho_i]$ in a basis chosen from a tomographically complete set. Using diluted maximum-likelihood estimation⁵⁵, the outcomes of the measurements can be used to reconstruct the χ -matrix representing the process. In practice, the input states are created by rotating $|0\rangle$ to $|\psi_i\rangle = R_i |0\rangle$ with

$$R_i \in \left\{ \mathbb{I}, \sigma_x, \frac{1}{\sqrt{2}}(\mathbb{I} - i\sigma_y), \frac{1}{\sqrt{2}}(\mathbb{I} + i\sigma_x) \right\}. \quad (2)$$

Likewise, the tomographic measurements are performed by rotating the output state $\mathcal{E}[\rho_i]$ by R_j [Eq. (2)], and subsequently measuring it in the σ_z basis. Ideally, this sequence implements the projectors $P_{0,j} = |\psi_j\rangle\langle\psi_j|$ and $P_{1,j} = |\psi_{\perp,j}\rangle\langle\psi_{\perp,j}|$, where $\langle\psi_{\perp,j}|\psi_j\rangle = 0$. However, SPAM errors would manifest as errors in the reconstructed process; we therefore model these errors by replacing the σ_z measurement with positive-operator-valued measures (POVMs),

$$\begin{aligned} M_0 &= (1 - \epsilon_{|0\rangle}) |0\rangle\langle 0| + \epsilon_{|1\rangle} |1\rangle\langle 1| \\ M_1 &= (1 - \epsilon_{|1\rangle}) |1\rangle\langle 1| + \epsilon_{|0\rangle} |0\rangle\langle 0|, \end{aligned}$$

where $\epsilon_{|0\rangle}$ ($\epsilon_{|1\rangle}$) is the SPAM error associated with the $|0\rangle$ ($|1\rangle$) qubit state. The values used for these operators are given in Ext. Fig. 2.

Resampling of the measurement outcomes is used to generate new data sets, which are analysed in the same way as the original data set, and are used to determine the sensitivity of the analysis to the statistical fluctuations in the input data. Error bars on the fidelities of reconstructed processes are quoted as the standard deviation of the fidelities of the resampled data sets.

Remote entanglement generation

The heralded generation of remote entanglement between network qubits in separate modules, outlined in Stephenson *et al.*²⁸, is central to our QGT protocol. Photons entangled with the Sr^+ ions are collected from each module using high-numerical aperture lenses and single-mode optical fibres bring the photons to a central Bell state analyser, where a measurement of the photons projects the ions into a maximally entangled state. This forms the photonic quantum channel interconnecting the two modules. Following Stephenson *et al.*²⁸, we use a 674 nm π -pulse to map the remote entanglement from the ground-state Zeeman qubit to an optical qubit, which we refer to as the network qubit, to minimise the number of quadrupole pulses in subsequent operations. Successful generation of entanglement is heralded by particular detector click patterns and, after subsequent local rotations, indicates the creation of the maximally entangled Ψ^+ Bell-state,

$$|\Psi^+\rangle = \frac{|10\rangle + |01\rangle}{\sqrt{2}} \in \mathcal{Q}_N^{\otimes 2}.$$

This process is executed while simultaneously storing quantum information in the circuit qubits which, as demonstrated by Drmota *et al.*³⁶, are robust to this network activity.

Each entanglement generation attempt takes 1168 ns and it takes 7084 attempts to successfully herald entanglement on average, corresponding to a success probability of 1.41×10^{-4} . To mitigate heating of the ion-crystal, we interleave 200 μs of entanglement generation attempts with 2.254 ms of sympathetic re-cooling of the Sr^+ - Ca^+ crystal using the Sr^+ ion. The sympathetic re-cooling comprises 1.254 ms of Doppler cooling, followed by 1 ms of electromagnetically-induced transparency (EIT) cooling. Overall, this results in an average entanglement generation rate of 9.7 s^{-1} (equivalently, it takes on average 103 ms to generate entanglement between network qubits), although this rate could be increased by optimising the interleaved cooling sequence. This rate is lower than the 182 s^{-1} rate previously reported in our apparatus²⁸ due to the additional cooling. We characterise

the remote entanglement using quantum state tomography; by performing tomographic measurements on 2×10^5 copies of the remotely entangled state, we reconstruct the density matrix of the network qubits, ρ_N^{AB} , shown in Ext. Fig. 3(d). In order to isolate the fidelity of the ‘‘Quantum Link’’ in Fig. 2, we account for the imperfect tomographic measurements in the reconstruction of the density matrix. The fidelity of the reconstructed state to the desired Ψ^+ Bell-state, given by $\langle \Psi^+ | \rho_N^{AB} | \Psi^+ \rangle$, is 97.15(9) %.

Circuit qubit memory during entanglement generation

Since each instance of QGT requires the generation of entanglement between network qubits, it is necessary to ensure that the circuit qubits preserve their encoded quantum information during this process. Due to their low sensitivity to magnetic field fluctuations, the circuit qubits have exhibited ~ 100 ms coherence times, and in previous work we demonstrated these qubits to be robust to network activity³⁶. We further suppress dephasing through dynamical decoupling. Typically, dynamical decoupling is implemented over a fixed period of time; however the success of the entanglement generation process is non-deterministic and would therefore leave the dynamical decoupling sequence incomplete.

One solution would be to complete the dynamical decoupling pulse sequence once the entanglement has been generated, however it is desirable to minimise the time between heralding the entanglement generation and performing the QGT protocol, in order to prevent dephasing of the network qubits. Instead, we make use of the fact that the action of a dynamical decoupling pulse on one of the circuit qubits can be propagated through the teleported CZ gate as

$$(X \otimes I)U_{\text{CZ}} = U_{\text{CZ}}(X \otimes Z). \quad (3)$$

We therefore perform the dynamical decoupling pulses on the circuit qubits until we obtain a herald of remote entanglement, at which point we immediately perform the QGT sequence – implementing a CZ gate on the state of the circuit qubits at the point of interruption. Once this gate is completed, we perform the remaining dynamical decoupling pulses (without any inter-pulse delay), and use (3) to apply the appropriate Z rotations required to correct for the propagation through the CZ gate. With this method, we suppress the dephasing errors in the circuit qubits during entanglement generation, while minimising the time between successfully heralding the entanglement and consuming it for QGT.

We deploy Knill dynamical decoupling^{56,57} with a 7.4 ms inter-pulse delay (corresponding to a pulse every three rounds of interleaved entanglement attempts and re-cooling). We use QPT to reconstruct the process of

storing the quantum information while generating entanglement; ideally, this process would not alter the quantum information stored in the circuit qubit. QPT is implemented by choosing input states for the circuit qubits from the tomographically complete set given in (1), generating remote entanglement between the network qubits while dynamically decoupling the circuit qubits, then upon successful herald, completing the dynamical decoupling sequence and performing tomographic measurements of the circuit qubits. The reconstructed process matrices for each module corresponding to the action of storing quantum information during entanglement generation are shown in Ext. Fig. 3(c). We observe fidelities to the ideal operation of 98.1(4) % and 98.2(5) % for Alice and Bob, respectively.

Local mixed-species entangling gates

The ability to perform logical entangling gates between ions of different species allows us to separate the roles of network and circuit ions. We implement mixed-species entangling gates following the approach taken by Hughes *et al.*³⁹, in which geometric phase gates are deterministically executed using a single pair of 402 nm Raman beams, as depicted in Ext. Fig. 4. Here, we apply the gate mechanism directly to the network qubit in Sr^+ – rather than the Zeeman ground state qubit, as done in Hughes *et al.*³⁹ and Drmota *et al.*³⁶ – at the cost of a slightly reduced gate efficiency that is compensated for by the use of higher laser powers. This enables us to perform mixed-species CZ gates between the network and auxiliary qubits. We characterise our mixed-species entangling gates using QPT in each module, reconstructing the process matrices χ_{CZ} representing the action of the local CZ gate acting between the network and auxiliary qubits. The reconstructed process matrices for each module are shown in Ext. Fig. 4(d). Compared to the ideal CZ gate, we observe average gate fidelities of 97.5(2) % and 98.0(2) % for Alice and Bob, respectively.

Hyperfine qubit transfer

Since the circuit qubit does not participate in the mixed-species gate, the gate interaction is performed on the network and auxiliary qubits. Consequently, we require the ability to map coherently between the circuit and auxiliary qubit before and after the local operations. As shown in Ext. Fig. 5, this mapping is performed using a pair of 402 nm Raman beams detuned by ~ 3.2 GHz, to coherently drive the transitions within the ground hyperfine manifold of Ca^+ .

The transfer of the circuit qubit to the auxiliary qubit begins with the mapping of the state $|0_{\text{C}}\rangle$ to the state $|0_{\text{X}}\rangle$. However, due to the near degeneracy of the tran-

sition $\mathcal{T}_0 : |0_{\text{C}}\rangle \leftrightarrow |F=3, M_F=+1\rangle$ and the transition $\mathcal{T}_1 : |1_{\text{C}}\rangle \leftrightarrow |F=4, M_F=+1\rangle$ (see Ext. Fig. 5), separated by only ~ 15 kHz, it is not possible to map the $|0_{\text{C}}\rangle$ state out of the circuit qubit without off-resonantly driving population out of the $|1_{\text{C}}\rangle$ state. We suppress this off-resonant excitation using a composite pulse sequence, shown in Ext. Fig. 5(b)(i), comprising three pulses resonant with the \mathcal{T}_0 transition, with pulse durations equal to the 2π -time of the \mathcal{T}_1 transition, and phases optimised to minimise the off-resonant excitation. This pulse sequence allows us to simultaneously perform a π -pulse on the \mathcal{T}_0 transition and the identity on the off-resonantly-driven \mathcal{T}_1 transition. Raman π -pulses are then used to complete the mapping to the $|0_{\text{X}}\rangle$ state. Another sequence of Raman π -pulses coherently maps $|1_{\text{C}}\rangle \rightarrow |1_{\text{X}}\rangle$, thereby completing the transfer of the circuit qubit to the auxiliary qubit, $\mathcal{Q}_{\text{C}} \rightarrow \mathcal{Q}_{\text{X}}$. To implement the mapping $\mathcal{Q}_{\text{X}} \rightarrow \mathcal{Q}_{\text{C}}$, the same pulse sequence is applied in reverse.

We characterise our $\mathcal{Q}_{\text{C}} \leftrightarrow \mathcal{Q}_{\text{X}}$ mapping sequence by performing a modification of single-qubit randomised benchmarking (RBM), in which we alternate Clifford operations on the \mathcal{Q}_{C} and \mathcal{Q}_{X} qubits, as illustrated in Ext. Fig. 5(c). We assume that (i) the single-qubit gate errors for the \mathcal{Q}_{C} and \mathcal{Q}_{X} qubits are negligible compared to the $\mathcal{Q}_{\text{C}} \leftrightarrow \mathcal{Q}_{\text{X}}$ transfer infidelity (we typically observe single-qubit gate errors $\sim 1 \times 10^{-4}$ for the Ca^+ hyperfine qubits), and (ii) the fidelity of the transfer $\mathcal{Q}_{\text{C}} \rightarrow \mathcal{Q}_{\text{X}}$ is similar to $\mathcal{Q}_{\text{X}} \rightarrow \mathcal{Q}_{\text{C}}$. We therefore model the survival probability as

$$S(m) = \frac{1}{2} + Bp^m$$

where m is the number of hyperfine transfers, B accounts for SPAM error offsets, and p is the depolarising probability for the transfer, related to the error per transfer as

$$\epsilon_{\text{C} \leftrightarrow \text{X}} = \frac{1-p}{2}.$$

The RBM results are shown in Ext. Fig. 5(c); we measure an error per transfer of $3.8(2) \times 10^{-3}$ ($2.6(1) \times 10^{-3}$) for Alice (Bob).

Conditional Operations

To complete the QGT protocol, the two modules perform mid-circuit measurements of the network qubits, exchange the measurement outcomes, and apply a local rotation of their circuit qubits conditioned on the outcomes of the measurements. By virtue of the spectral isolation between the two species of ions, mid-circuit measurements of the network qubits can be made without affecting the quantum state of the circuit qubits. The mid-circuit measurement outcomes, $m_{\text{A}}, m_{\text{B}} \in \{0, 1\}$, are exchanged in real-time via a classical communication channel between the modules – in our demonstration, this is

a TTL link connecting the control systems of the two modules. Following the exchange of the measurement outcomes, the modules, Alice and Bob, perform the conditional rotations U_A and U_B , respectively, where

$$U_A = \begin{cases} S^\dagger & \text{if } m_A \oplus m_B = 0, \\ S & \text{otherwise,} \end{cases}$$

$$U_B = \begin{cases} S & \text{if } m_A \oplus m_B = 0, \\ S^\dagger & \text{otherwise,} \end{cases}$$

where $S = \text{diag}(1, i)$.

Errors in the mid-circuit measurements of the network qubits will result in the application of the wrong conditional rotation; effectively, this would appear as a joint phase-flip of the circuit qubits following the teleported gate. The mid-circuit measurement errors arise from the non-ideal single-qubit rotation of the network qubit to map the measurement basis onto the computational basis, and errors due to the fluorescence detection of the network qubit. Using RBM, we measure single-qubit gate errors for the network qubits of $4.8(3) \times 10^{-4}$ and $9.8(3) \times 10^{-4}$ for Alice and Bob, respectively. The error in the fluorescence detection is estimated from the observed photon scattering rates of \mathcal{Q}_N states, in addition to the ≈ 390 ms lifetime of the $|1_N\rangle$ state⁵⁸. We choose a mid-circuit measurement duration of 500 μ s; we estimate fluorescence detection errors of $6.6(1) \times 10^{-4}$ and $5.51(2) \times 10^{-4}$ for Alice and Bob, respectively. Combining these error mechanisms, we estimate contributions to the teleported CZ gate error of 0.091(3) % and 0.122(2) % for Alice and Bob, respectively.

* dougal.main@physics.ox.ac.uk

- [1] Grover, L. K., Quantum teleportation. Preprint at <https://arxiv.org/abs/quant-ph/9704012> (1997).
- [2] Cirac, J. I., Ekert, A. K., Huelga, S. F. & Macchiavello, C. Distributed quantum computation over noisy channels. *Phys. Rev. A* **59**, 4249 (1999).
- [3] Jiang, L., Taylor, J. M., Sørensen, A. S. & Lukin, M. D. Distributed quantum computation based on small quantum registers. *Phys. Rev. A* **76**, 062323 (2007).
- [4] Monroe, C. *et al.* Large-scale modular quantum-computer architecture with atomic memory and photonic interconnects. *Phys. Rev. A* **89**, 022317 (2014).
- [5] Grover, L. K. A fast quantum mechanical algorithm for database search. In *Proceedings of the Twenty-Eighth Annual ACM Symposium on Theory of Computing*, STOC '96 (Association for Computing Machinery, New York, NY, USA, 1996) p. 212–219.
- [6] Vidal, G. & Dawson, C. M. Universal quantum circuit for two-qubit transformations with three controlled-not gates. *Phys. Rev. A* **69**, 010301 (2004).
- [7] Shor, P. W. Polynomial-time algorithms for prime factorization and discrete logarithms on a quantum computer. *SIAM J. Comput.* **26**, 1484–1509 (1997).
- [8] Cao, Y., Romero, J. & Aspuru-Guzik, A. Potential of quantum computing for drug discovery. *IBM J. Res. Dev.* **62**, 6:1 (2018).
- [9] Bruzewicz, C. D., Chiaverini, J., McConnell, R. & Sage, J. M. Trapped-ion quantum computing: Progress and challenges. *Appl. Phys. Rev.* **6**, 021314 (2019).
- [10] Bravyi, S., Dial, O., Gambetta, J. M., Gil, D. & Nazario, Z. The future of quantum computing with superconducting qubits. *J. Appl. Phys.* **132**, 160902 (2022).
- [11] Gill, S. S. *et al.*, Quantum computing: Vision and challenges. Preprint at <https://arxiv.org/abs/2403.02240> (2024).
- [12] Bennett, C. H. *et al.* Teleporting an unknown quantum state via dual classical and Einstein-Podolsky-Rosen channels. *Phys. Rev. Lett.* **70**, 1895 (1993).
- [13] Gottesman, D. & Chuang, I. L. Demonstrating the viability of universal quantum computation using teleportation and single-qubit operations. *Nature* **402**, 390 (1999).
- [14] Eisert, J., Jacobs, K., Papadopoulos, P. & Plenio, M. B. Optimal local implementation of nonlocal quantum gates. *Phys. Rev. A* **62**, 052317 (2000).
- [15] Collins, D., Linden, N. & Popescu, S. Nonlocal content of quantum operations. *Phys. Rev. A* **64**, 032302 (2001).
- [16] Briegel, H.-J., Dür, W., Cirac, J. I. & Zoller, P. Quantum repeaters: The role of imperfect local operations in quantum communication. *Phys. Rev. Lett.* **81**, 5932 (1998).
- [17] Dür, W. & Briegel, H.-J. Entanglement purification for quantum computation. *Phys. Rev. Lett.* **90**, 067901 (2003).
- [18] Kielpinski, D., Monroe, C. & Wineland, D. J. Architecture for a large-scale ion-trap quantum computer. *Nature* **417**, 709 (2002).
- [19] Akhtar, M. *et al.* A high-fidelity quantum matter-link between ion-trap microchip modules. *Nat. Commun.* **14**, 531 (2023).
- [20] Wan, Y. *et al.* Quantum gate teleportation between separated qubits in a trapped-ion processor. *Science* **364**, 875 (2019).
- [21] Pino, J. M. *et al.* Demonstration of the trapped-ion quantum CCD computer architecture. *Nature* **592**, 209 (2021).
- [22] Humphreys, P. C. *et al.* Deterministic delivery of remote entanglement on a quantum network. *Nature* **558**, 268 (2018).
- [23] Knaut, C. M. *et al.* Entanglement of nanophotonic quantum memory nodes in a telecom network. *Nature* **629**, 573 (2024).
- [24] Storz, S. *et al.* Loophole-free Bell inequality violation with superconducting circuits. *Nature* **617**, 265 (2023).
- [25] Ritter, S. *et al.* An elementary quantum network of single atoms in optical cavities. *Nature* **484**, 195 (2012).
- [26] van Leent, T. *et al.* Entangling single atoms over 33 km telecom fibre. *Nature* **607**, 69 (2022).
- [27] Moehring, D. L. *et al.* Entanglement of single-atom quantum bits at a distance. *Nature* **449**, 68 (2007).
- [28] Stephenson, L. J. *et al.* High-rate, high-fidelity entanglement of qubits across an elementary quantum network. *Phys. Rev. Lett.* **124**, 110501 (2020).
- [29] Saha, S. *et al.*, High-fidelity remote entanglement of trapped atoms mediated by time-bin photons. Preprint

- at <https://arxiv.org/abs/2406.01761> (2024).
- [30] Huang, Y.-F., Ren, X.-F., Zhang, Y.-S., Duan, L.-M. & Guo, G.-C. Experimental teleportation of a quantum controlled-not gate. *Phys. Rev. Lett.* **93**, 240501 (2004).
- [31] Gao, W.-B. *et al.* Teleportation-based realization of an optical quantum two-qubit entangling gate. *Proc. Natl. Acad. Sci. U.S.A.* **107**, 20869 (2010).
- [32] Chou, K. S. *et al.* Deterministic teleportation of a quantum gate between two logical qubits. *Nature* **561**, 368 (2018).
- [33] Bäumer, E. *et al.*, Efficient long-range entanglement using dynamic circuits. Preprint at <https://arxiv.org/abs/2308.13065> (2023).
- [34] Hashim, A. *et al.*, Efficient generation of multi-partite entanglement between non-local superconducting qubits using classical feedback. Preprint at <https://arxiv.org/abs/2403.18768> (2024).
- [35] Daiss, S. *et al.* A quantum-logic gate between distant quantum-network modules. *Science* **371**, 614 (2021).
- [36] Drmota, P. *et al.* Robust quantum memory in a trapped-ion quantum network node. *Phys. Rev. Lett.* **130**, 090803 (2023).
- [37] Harty, T. P. *et al.* High-fidelity trapped-ion quantum logic using near-field microwaves. *Phys. Rev. Lett.* **117**, 140501 (2016).
- [38] Ballance, C. J., Harty, T. P., Linke, N. M., Sepiol, M. A. & Lucas, D. M. High-fidelity quantum logic gates using trapped-ion hyperfine qubits. *Phys. Rev. Lett.* **117**, 060504 (2016).
- [39] Hughes, A. C. *et al.* Benchmarking a high-fidelity mixed-species entangling gate. *Phys. Rev. Lett.* **125**, 080504 (2020).
- [40] Srinivas, R. *et al.* High-fidelity laser-free universal control of trapped ion qubits. *Nature* **597**, 209 (2021).
- [41] Moses, S. A. *et al.* A race-track trapped-ion quantum processor. *Phys. Rev. X* **13**, 041052 (2023).
- [42] Weber, M. A. *et al.*, Robust and fast microwave-driven quantum logic for trapped-ion qubits. Preprint at <https://arxiv.org/abs/2402.12955> (2024).
- [43] Nigmatullin, R., Ballance, C. J., de Beaudrap, N. & Benjamin, S. C. Minimally complex ion traps as modules for quantum communication and computing. *New J. Phys.* **18**, 103028 (2016).
- [44] Hilder, J. *et al.* Fault-tolerant parity readout on a shuttling-based trapped-ion quantum computer. *Phys. Rev. X* **12**, 011032 (2022).
- [45] Knollmann, F. W. *et al.*, Integrated photonic structures for photon-mediated entanglement of trapped ions. Preprint at <https://arxiv.org/abs/2401.06850> (2024).
- [46] Luo, Y.-H. *et al.* Quantum teleportation in high dimensions. *Phys. Rev. Lett.* **123**, 070505 (2019).
- [47] Lloyd, S. & Braunstein, S. L. Quantum computation over continuous variables. *Phys. Rev. Lett.* **82**, 1784 (1999).
- [48] Walshe, B. W., Baragiola, B. Q., Alexander, R. N. & Menicucci, N. C. Continuous-variable gate teleportation and bosonic-code error correction. *Phys. Rev. A* **102**, 062411 (2020).
- [49] Wehner, S., Elkouss, D. & Hanson, R. Quantum internet: A vision for the road ahead. *Science* **362**, eaam9288 (2018).
- [50] Hillery, M., Bužek, V. & Berthiaume, A. Quantum secret sharing. *Phys. Rev. A* **59**, 1829 (1999).
- [51] Kómár, P. *et al.* A quantum network of clocks. *Nat. Phys.* **10**, 582 (2014).
- [52] Greenberger, D. M., Horne, M. A., Shimony, A. & Zeilinger, A. Bell's theorem without inequalities. *Am. J. Phys.* **58**, 1131 (1990).
- [53] Maunz, P. L. W. High optical access trap 2.0. 10.2172/1237003 (2016).
- [54] Revelle, M. C., Phoenix and Peregrine ion traps. Preprint at <https://arxiv.org/abs/2009.02398> (2020).
- [55] Řeháček, J., Hradil, Z., Knill, E. & Lvovsky, A. I. Diluted maximum-likelihood algorithm for quantum tomography. *Phys. Rev. A* **75**, 042108 (2007).
- [56] Wang, P. *et al.* Single ion qubit with estimated coherence time exceeding one hour. *Nat. Commun.* **12**, 233 (2021).
- [57] Souza, A. M., Álvarez, G. A. & Suter, D. Robust dynamical decoupling for quantum computing and quantum memory. *Phys. Rev. Lett.* **106**, 240501 (2011).
- [58] Letchumanan, V., Wilson, M. A., Gill, P. & Sinclair, A. G. Lifetime measurement of the metastable $4d^2D_{5/2}$ state in $^{88}\text{Sr}^+$ using a single trapped ion. *Phys. Rev. A* **72**, 012509 (2005).
- [59] Bourdeauducq, S. *et al.*, m-labs/artiq: 6.0 (Version 6.0) (2021).

ACKNOWLEDGEMENTS

We thank Oana Băzăvan, Sebastian Saner, and Donovan Webb for maintenance of the 674-nm laser system. We thank Chris Ballance and Laurent Stephenson for design of the apparatus, Péter Juhász for comments on the manuscript, Sandia National Laboratories for supplying the ion traps used in this experiment, and the developers of the control system ARTIQ⁵⁹. DM acknowledges support from the U.S. Army Research Office (ref. W911NF-18-1-0340). DPN acknowledges support from Merton College, Oxford. EMA acknowledges support from the U.K. EPSRC “Quantum Communications” Hub EP/T001011/1. RS acknowledges funding from an EPSRC Fellowship EP/W028026/1 and Balliol College, Oxford. GA acknowledges support from Wolfson College, Oxford. This work was supported by the U.K. EPSRC “Quantum Computing and Simulation” Hub EP/T001062/1.

AUTHOR INFORMATION

Contributions

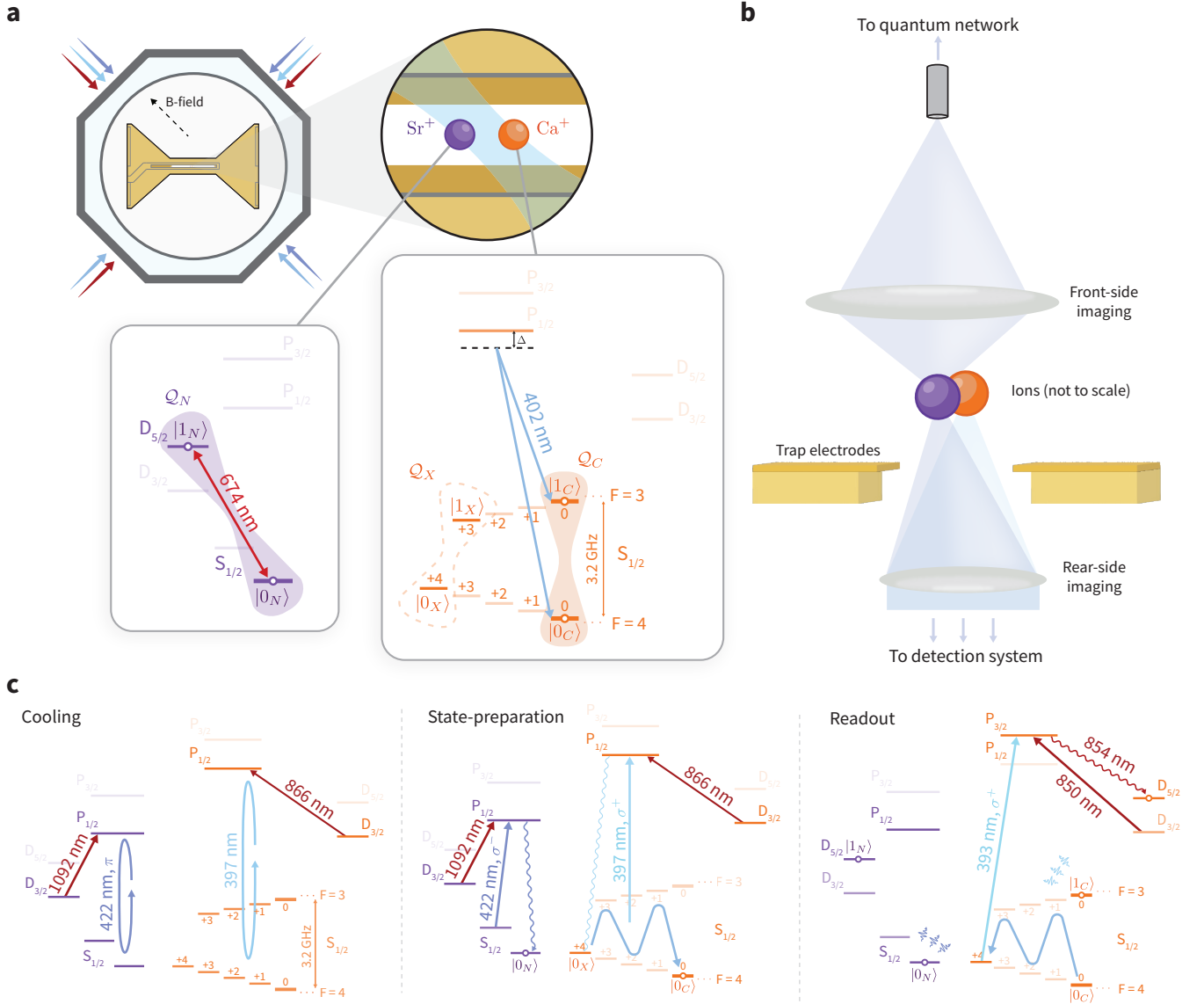
DM, PD, DPN, EMA, AA, BCN, RS, GA built and operated the experimental apparatus. DM led the experimental work, with assistance from PD and DPN. DM performed the data analysis and prepared the manuscript with input from all authors. DML secured funding and supervised the work. All authors contributed to the discussion and interpretation of results.

Competing Interests

RS is partially employed by Oxford Ionics Ltd. The remaining authors declare no competing interests.

Corresponding Authors

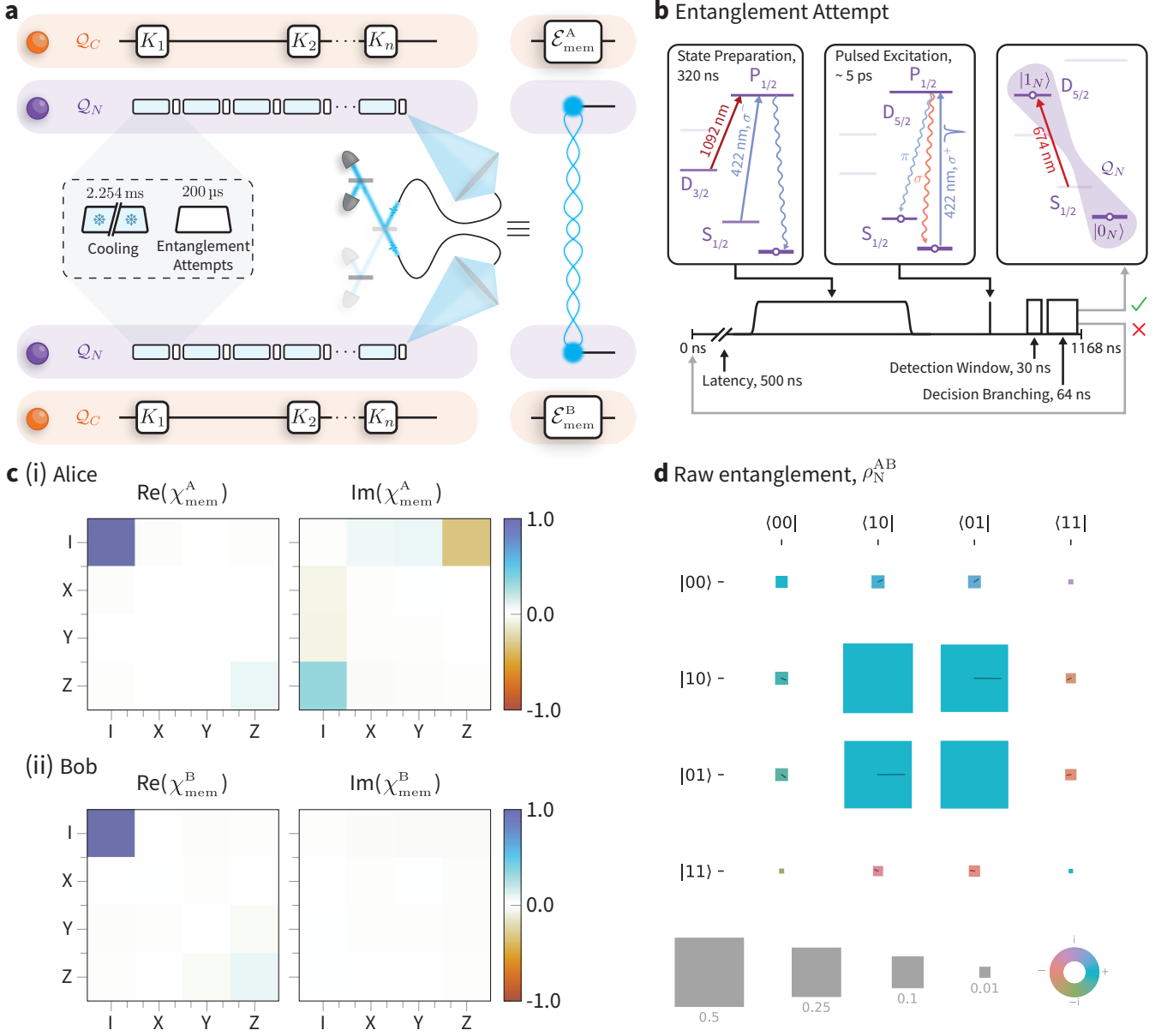
Correspondence should be addressed to DM or DML.



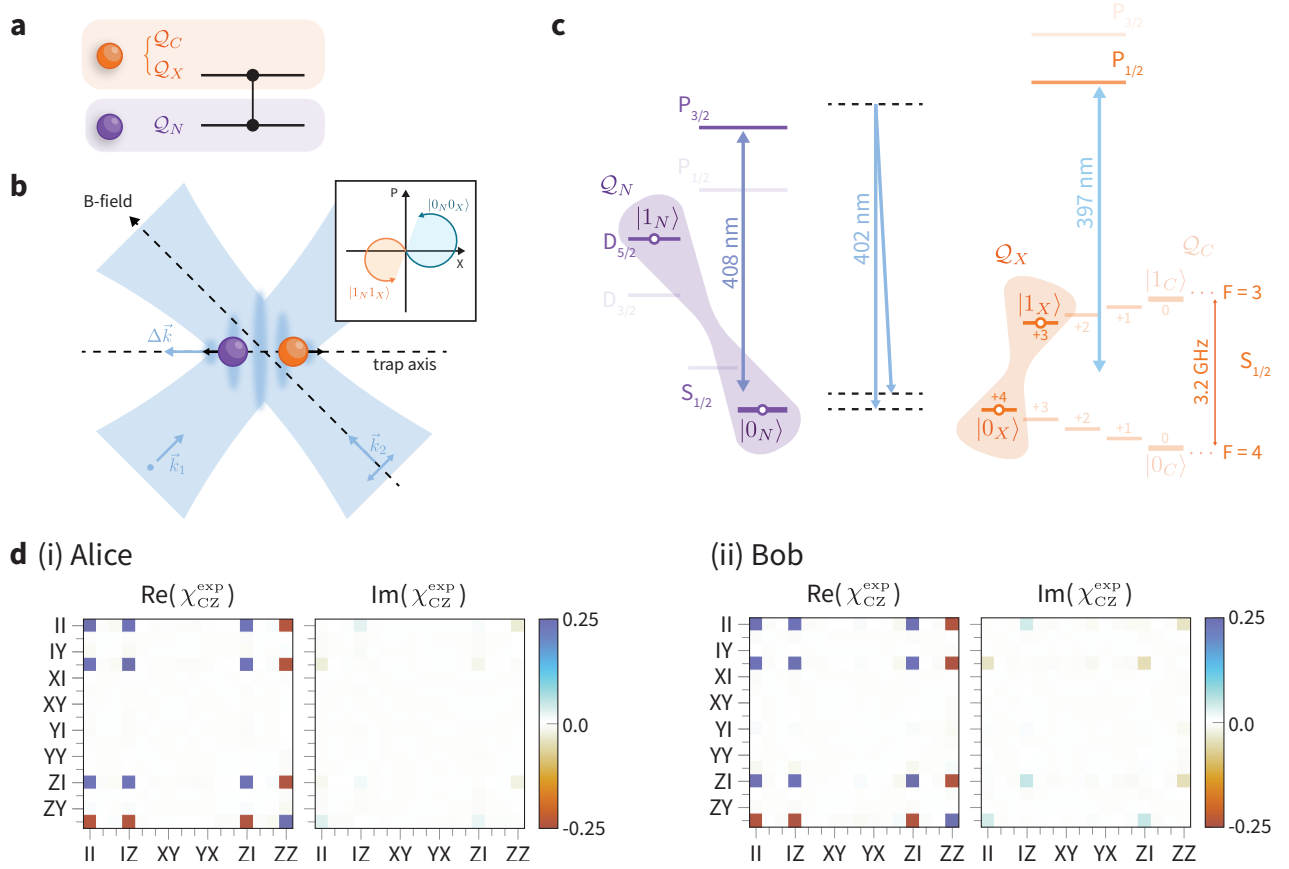
Ext. Fig. 1. Outline of a trapped-ion module. **a**, An ultra-high vacuum chamber houses a micro-fabricated surface Paul trap, which co-traps one $^{88}\text{Sr}^+$ ion and one $^{43}\text{Ca}^+$ ion. The ions are manipulated using lasers, which are delivered parallel to the surface of the trap. The Sr^+ ion provides an optical network qubit, Q_N , which is coherently manipulated using a 674 nm laser. The ground hyperfine manifold of the Ca^+ ion provides a circuit qubit, Q_C , and an auxiliary qubit, Q_X . The qubits in the ground hyperfine manifold are addressed using a pair of 402 nm Raman beams. **b**, The rear-side imaging system is used to perform fluorescence detection for qubit readout of both species. The front-side imaging system is used for single-photon collection from the Sr^+ ion during the generation of entanglement. A high-numerical aperture (0.6 NA) lens couples the single-photons into a single-mode optical fibre, which connects to the optical quantum network. Both imaging systems are outside the vacuum chamber. **c**, Energy level diagrams for cooling, state-preparation, and readout of each species. For state preparation and readout of the circuit qubit Q_C in Ca^+ , we utilise the auxiliary qubit Q_X . During state preparation, we prepare $|0_X\rangle$ via optical pumping and then transfer it to $|0_C\rangle$ using Raman π -pulses. For readout, we transfer $|0_C\rangle$ to $|0_X\rangle$ before shelving to the $D_{5/2}$ manifold. Fluorescence detection is then used for both species, to indicate whether the ion is shelved.

Module	Qubit	$\epsilon_{ 0\rangle} (\times 10^{-3})$	$\epsilon_{ 1\rangle} (\times 10^{-3})$
Alice	Network qubit, \mathcal{Q}_N	2.6(6)	7.8(8)
	Circuit qubit, \mathcal{Q}_C	8.5(9)	6.4(6)
	Auxiliary qubit, \mathcal{Q}_X	4.7(7)	3.6(4)
Bob	Network qubit, \mathcal{Q}_N	6.5(8)	4.5(6)
	Circuit qubit, \mathcal{Q}_C	6.0(8)	7.5(6)
	Auxiliary qubit, \mathcal{Q}_X	3.2(7)	5.3(5)

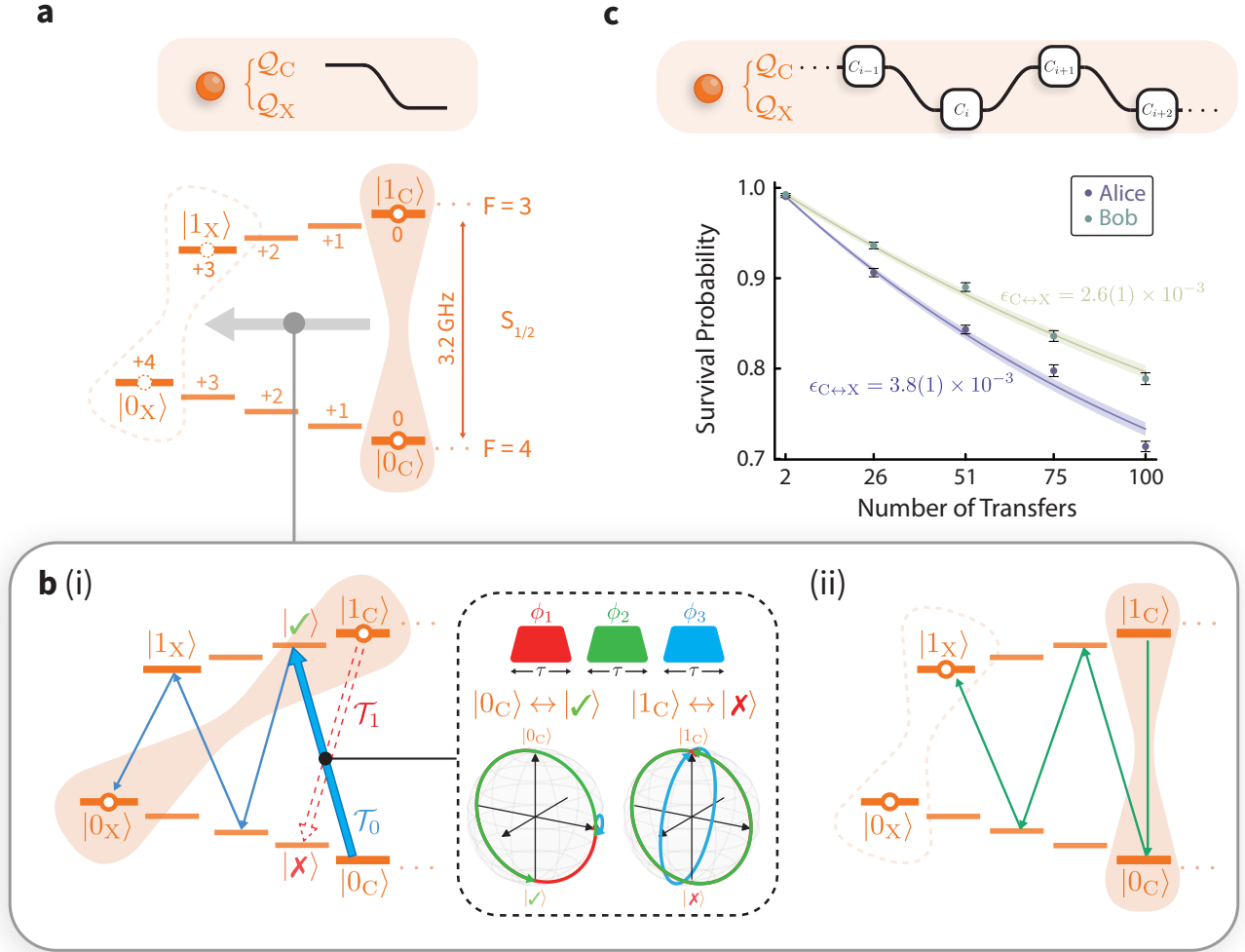
Ext. Fig. 2. State-preparation and measurement errors for all of the qubit states, in each module. The average SPAM error is $5.0(2) \times 10^{-3}$.



Ext. Fig. 3. Generation of remote entanglement and robust memory of the circuit qubits. **a**, Entanglement is generated between the network qubits using 200 μ s of entanglement attempts interleaved with 2.254 ms of sympathetic re-cooling using the Sr^+ ion. This is repeated until the entanglement is successfully heralded by a particular detector click pattern. While attempting to generate entanglement between the network qubits, Knill dynamical decoupling pulses, K_i , are used to preserve the state of the circuit qubits. **b**, Each entanglement attempt has a total duration of 1168 ns. We perform a 320 ns state-preparation pulse (which has a switching latency of 500 ns), pumping the Sr^+ ion into the lower ground Zeeman state. A ~ 5 ps pulse excites the Sr^+ ion to the upper $P_{1/2}$ level, which rapidly decays to one of the ground Zeeman levels (lifetime ~ 7 ns), thereby generating ion-photon entanglement. We collect a photon from each of the modules, interfere them on a beamsplitter, and perform a projective measurement on the two-photon polarisation state. Particular detector click patterns occurring within the detection window herald the successful generation of remote entanglement. We then exit the attempt loop and map the entanglement into the optical network qubits, Q_N . **c**, Reconstructed process matrices for the process of storing the state of the circuit qubit in (i) Alice and (ii) Bob while generating entanglement on the network qubits. The reconstructed process matrices have fidelities 98.1(4) % and 98.2(5) % for Alice and Bob, respectively. **d**, Reconstructed density matrix of the remotely entangled network qubits. The state indicates a fidelity of 97.15(9) % to the $|\Psi^+\rangle$ Bell state.



Ext. Fig. 4. Implementation of the local mixed-species CZ gates. **a**, Circuit element for the local CZ gate, implemented between the Q_N and Q_X qubits. **b**, Geometry for the mixed-species gate mechanism. A pair of Raman lasers are aligned orthogonal to one another, such that their relative wavevector, $\Delta\vec{k}$ is along the trap axis. The interference of these beams gives rise to a polarisation travelling-standing wave which induces spin-dependent light-shifts oscillating at a frequency close to the frequency of the axial out-of-phase motional mode. The ions therefore experience a spin-dependent force that displaces the spin states in phase space, as depicted in the inset, thus enabling the implementation of geometric phase gates. **c**, Energy level diagram for the gate mechanism acting on the Q_N and Q_X qubits. By tuning the Raman lasers to 402 nm, we couple to both the 397 nm $S_{1/2} \leftrightarrow P_{1/2}$ dipole transition in Ca^+ and the 408 nm $S_{1/2} \leftrightarrow P_{3/2}$ dipole transition in Sr^+ . **d** Process matrices for the local, mixed-species CZ gates for (i) Alice and (ii) Bob. The process matrices have average gate fidelities of 97.5(2)% and 98.0(2)% for Alice and Bob, respectively.



Ext. Fig. 5. Transfer between the circuit and auxiliary qubits. **a**, Circuit element and level diagram depicting the coherent transfer of quantum information from the \mathcal{Q}_C qubit to the \mathcal{Q}_X qubit. The inverse transfer is implemented by performing the same steps in reverse. **b**, The transfer pulse sequence comprises two steps. (i) The first step maps the state $|0_C\rangle$ to $|0_X\rangle$. Due to the near-degeneracy of the intended transition $\mathcal{T}_0 : |0_C\rangle \leftrightarrow |\checkmark\rangle$ (thick blue arrow) and the unwanted transition $\mathcal{T}_1 : |1_C\rangle \leftrightarrow |\times\rangle$ (red dashed arrow), separated by only ~ 15 kHz, we employ a composite pulse sequence to suppress off-resonant coupling to the \mathcal{T}_1 transition. The composite pulse sequence, shown in the dashed box, comprises 3 pulses of duration τ resonant with the \mathcal{T}_0 transition with differing phases ϕ_i . The pulse duration, τ , is equal to the 2π -time of the \mathcal{T}_1 transition, $\phi_1 = \phi_3 = 0$, and $\phi_2 \approx 2\pi \times 0.231$ is optimised experimentally. The subsequent transfer pulses (thin blue arrows) are π -pulses on the relevant transitions. This sequence therefore performs the mapping $|0_C\rangle \rightarrow |0_X\rangle$, while leaving the state $|1_C\rangle$ unaffected. (ii) The second step comprises a sequence of π -pulses which maps $|1_C\rangle \rightarrow |1_X\rangle$. This completes the coherent transfer $\mathcal{Q}_C \rightarrow \mathcal{Q}_X$. **c**, The performance of the transfer sequence is characterised using a modified version of RBM in which we alternately perform Clifford operations on the \mathcal{Q}_C and \mathcal{Q}_X qubits. By measuring the survival probability for different numbers of transfers, and neglecting the errors of the single-qubit gates C_i (which are $\sim 1 \times 10^{-4}$), we extract the error per transfer, $\epsilon_{C \leftrightarrow X}$, yielding $3.8(2) \times 10^{-3}$ and $2.6(1) \times 10^{-3}$ for Alice and Bob, respectively.